

The Morphology of the 3-6 keV Continuum and Fe-K α Emission of the Compton Thick AGN NGC 3393

Kieran Parker,^{1,2}

¹*Physics and Astronomy, University of Southampton, Highfield, SO17 1BJ, UK*

²*Center for Astrophysics | Harvard & Smithsonian, 60 Garden Street, Cambridge MA 02138, USA*

15 May 2019

ABSTRACT

Active Galactic Nuclei have very luminous centres that cannot be explained by stellar emission. It is assumed that this emission travels to a flattened region of material around the accretion disk known as the torus and through the torus opening, out to interstellar medium (ISM) clouds. For us to be able to observe the hard X-ray component of this emission, it needs to be scattered into our line of sight by Compton thick (CT) clouds, beyond the torus and ISM clouds. I present a morphological analysis of this hard X-ray emission in the CT AGN NGC 3393 to look for extended emission via comparison with a simulation of Chandra's point spread function. Extended emission is found in the cone (perpendicular to the plane of the torus) in the soft X-rays (0.3 keV - 3.0 keV) and in the hard X-ray continuum (3.0 keV - 6.0 keV). In the cross-cone (parallel to the plane of the torus) extended emission is detected in the soft X-rays. It is known that the soft X-ray emission is extended but the hard X-ray emission being extended at small radii is a new discovery. It likely means that there are CT clouds near the central source of emission and outside the torus to scatter the hard X-rays. At larger distances away from the nuclear source the cone and cross-cone emission are both extended in the soft X-rays. In the hard X-ray continuum, the cone is extended up to 6.0 keV and the cross-cone up to 5.0 keV, both out to 7 kpc. Neither the cone nor cross-cone emission is extended in the Fe-K α emission line at \sim 6.4 keV. This cross-cone extent suggests that the torus may not be a uniformly dense material. This evidence supports the findings of others and argues that the uniformly dense model of the torus that was widely accepted should be updated to instead be made up of a clumpy structure. Another possibility for this cross-cone extent, suggested by recent simulations, is that it may be due to the interaction of the radio jet with the molecular disk of the galaxy, causing X-ray hot bubbles in the cross-cone direction.

Key words: galaxies: individual (NGC 3393) — galaxies: ISM — galaxies: jets — galaxies: Seyfert — X-rays: general

1 INTRODUCTION

1.1 AGN Emission

An Active Galactic Nucleus (AGN) is the extremely luminous nuclear source of a galaxy whose emission cannot be explained by stellar processes. This luminosity is believed to be due to the interaction between a massive or supermassive black hole (SMBH) at the centre of the AGN and an accretion disk (AD) which feeds it (Rees 1984). In AGNs the AD mostly emits in the blue and UV, known as the blue bump, but the surrounding regions can also emit in X-rays. The X-ray photons are thought to originate in a region above the

accretion disk known as the corona. A few possibilities of the mechanisms producing these photons are that the UV photons from the accretion disk get inverse Compton boosted in the corona to much higher energies (e.g. X-rays) or due to the high magnetic field, close to the event horizon, accelerating electrons (Zamaninasab et al. 2014). Synchrotron radiation could be the source of the X-rays photons. Magnetic fields are also thought to be instrumental in producing the radio jets which are emitted from this inner region. Optical emission is observed from AGN in two types of emission lines: broad lines and narrow lines.

As can be seen in Figure 1, a torus of dusty molecular

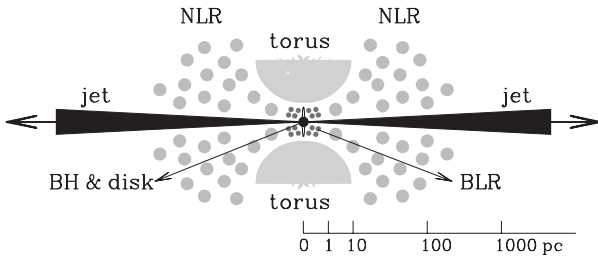


Figure 1. Cross section showing the structure of an AGN. (Mo et al. 2010)

clouds may feed this accretion disk. This torus is typically up to tens of parsecs (pc) (see Barvainis 1987). In Compton Thick (CT) AGNs, this torus has a radial column density of at least the inverse of the Thomson scattering cross-section, $N_{\text{H}} \geq 1.5 \times 10^{24} \text{ cm}^{-2}$, which leads to absorption of the X-ray photons, which warms the torus (Comastri 2004). A uniform CT torus will have an optical depth of $\tau_c \gg 1$, therefore the number of X-ray photons that are scattered into the line of sight of the observer is $\propto 1/e^{\tau_c}$. Therefore the larger the optical depth of a torus, the fewer photons make it into the observer's line of sight. However some hard (>3 keV) X-rays can be scattered into our line of sight by the CT clouds and Fe-K α emission, at ~ 6.4 keV, is produced by fluorescence (Matt et al. 1996). Until recently this hard continuum and Fe-K α line were thought to be confined to the torus or the area around it (see Marinucci et al. 2012).

The original Unified Model of AGN used the torus to explain the many different properties of AGNs using two parameters; the inclination of the torus to the line of sight and the AGN luminosity (e.g. Antonucci 1993). Seyfert Type IIs are AGNs where due to our edge-on line of sight, the nuclear source and the broad optical emission lines are obscured by the optically thick torus. The narrow emission lines associated with Seyfert Type II AGNs originate from stimulated and collisionally excited emission in a narrow line region (NLR) which is situated in a photoionised biconical region known as the ionisation cones (see Kraemer et al. 2000). Some of these lines are from the UV and soft X-rays emitted from and near the accretion disk, photoionising the interstellar medium (ISM) clouds. It is typical for this NLR to be extended up to kiloparsec size (Maksym et al. 2016).

There are a number of possibilities for the origin of these clouds. They could be ISM clouds that are in the host galaxy or they could be formed from matter being driven away from the accretion disk, in a phenomenon known as AD winds. These winds could be formed from a process that is analogous to the process in asymptotic giant branch stars therefore dust forms at the outer edge of the AD. Due to the dust's high opacity, it experiences a strong force from the predominately UV radiation being emitted by the AD. The pressure builds up until the pressure force overcomes the gravitational force and this dust is blown away in an AD wind. Another possible method is analogous to the stellar winds produced in Wolf-Rayet and O type stars.

Overall, the X-ray emission from these AGNs is spectrally complex. The soft band (<3.0 keV) is rich in emission lines and is typically extended (Levenson et al. 2006). There is close correspondence between soft X-rays and the narrow

emission line region (Wang et al. 2011 and Paggi et al. 2012). The hard (>3.0 keV) X-ray emission has a mostly featureless spectrum ('continuum') except for a strong Fe-K α line at ~ 6.4 keV in CT AGN (see Levenson et al. 2006). Due to their higher energy, the hard X-rays will pass through the NLR but more recently it has been discovered that this emission is extended in the ionisation cones as well (Arévalo et al. 2014). This is due to a scattering interaction with the interstellar medium (ISM) clouds, which have a higher density than those in the NLR allowing for this process to happen.

Fabbiano et al. 2017 has recently shown hard (3.0 keV - 6.0 keV) and Fe-K α line (~ 6.4 keV) extended X-ray emission in ESO 428-G014 in the direction of the opening of the torus in a region co-spatial with the soft extended X-ray emission of the ionised bi-cone. This extended hard radiation implies scattering from dense clouds in the disk of the host galaxy.

In a recent review of the Unified Model of AGNs, it has been suggested that the torus has a more complicated structure than previously thought. The current understanding is that the torus is not uniform but instead is made up of a clumpy composition of dusty molecular gas (Netzer 2015). Therefore, this would mean that some regions of the torus are not Compton thick and would allow for X-ray photons to pass through these regions of torus, to then be scattered into our line of sight. This would be detected by the observer as cross-cone extended emission, which is one feature I will be searching for in the following galaxy. Even more recently it has been suggested through simulations that this cross-cone extended emission could be due to the interaction of the radio jet with the molecular disk of the galaxy (Mukherjee et al. 2018).

1.2 NGC 3393

For this thesis, I have studied NGC 3393, which is a CT Seyfert Type II AGN (Maiolino et al. 1998). It lies at a distance of ~ 53 Mpc (Maksym et al. 2016 from Theureau et al. 1998) so $1'' \sim 279$ pc. A Seyfert Type II AGN was observed with Chandra ACIS due to the obscuration of the nuclear source, which allows for the fainter extended emission to be observed. In unobscured Type I AGN this emission would be drowned out due to the bright nuclear X-rays.

An approximate value for the size of the torus in NGC 3393 can be calculated using constraints on the dust distribution in the AGN, and more specifically, the equation

$$r = 1.3 L_{\text{uv},46}^{1/2} T_{1500}^{-2.8} \text{ pc} \quad (1)$$

where $L_{\text{uv},46}^{1/2}$ is the total ultraviolet luminosity in units of 10^{46} ergs s $^{-1}$ and $T_{1500}^{-2.8}$ is the grain evaporation temperature in units of 1500K (Barvainis 1987).

A typical value for the temperature of the inner edge of the torus is 1500K. The torus cools as the distance from the SMBH increases leading to a temperature on the outer edge of the torus to be 150K. The accretion disk predominantly emits in UV which heats up the particles in the dusty torus. This heating leads to the re-emission of the UV as IR radiation. Therefore the intrinsic luminosity of IR in the torus can be used as a proxy for the intrinsic UV luminosity. For NGC 3393 this is 10^{44} ergs s $^{-1}$ (Levenson et al. 2006) and therefore using equation 1 the radius of the inner edge of the torus is at ~ 0.13 pc. Using the value of 150K at the

outer edge results in a radius of ~ 82 pc, giving the torus an approximate diameter of 160 pc.

An analysis of the X-ray emission from the CT AGN NGC 3393 should be able to show if this torus model is either uniform or clumpy. If there is extended emission in the cross-cone region, especially in the hard continuum (3.0 keV - 6.0 keV), then the torus may be clumpy.

It has been demonstrated that this could be the case in the Seyfert Type II galaxy ESO 428-G014 (Fabbiano et al. 2018). X-ray emission from the torus region should only be on the scale of a few ten parsecs. This work discovered kiloparsec scale emission in the hard X-ray continuum and the Fe-K α emission line in the cross-cone (parallel to the torus) directions. This diffuse emission, present in both the cone and cross-cone, became less extended at higher energies, although showing a slight increase in extent for the Fe-K α line in the ionized cones. This extent was seen up to ~ 3 kpc.

Similar work on NGC 3393 has shown evidence of reprocessing of photoionisation which has passed through the torus in the radial direction, providing evidence of a clumpy model. This suggests that there is extended emission from this AGN, in the soft bands at least (Maksym et al. 2019). Maksym et al. (2019) also visually found extended hard emission using an exposure of 98.49 ks whereas the exposure used in this work is over 3 times that. There have been more discoveries of cross-cone kpc extended emission in NGC 4151 (Wang et al. 2011) and in Markarian 573 (Paggi et al. 2012). In Markarian 573, it has been shown that there is ~ 13 kpc of soft X-ray extended emission in the ionization cones and ~ 9 kpc in the cross-cones, suggesting that the radiation has travelled through the Compton thick torus.

I studied the Chandra ACIS-S images of NGC 3393 in several energy bands. I produced images and determined the radial profiles of the emission for the surface brightness of NGC 3393 across statistically appropriate energy bands, from 0.3 keV - 6.6 keV, including the Fe-K α line at ~ 6.4 keV. In comparison with the Chandra PSF, this allows for the determination of which energy band is most extended and therefore this can provide clues on the origin of this extended emission. These were compared with radial profiles of surface brightness from a simulated point spread function (PSF) to determine if and where there was extended emission. By taking the FWHM I was able to determine any possible trends in the extended emission when comparing the ionized cones to the cross-cone regions.

This study looks to support the results of the hard extended features in ESO 428-G014 found by Fabbiano et al., to investigate this newly discovered extended hard emission and possibly provide more supporting evidence for a need for a new torus model to become more universally accepted.

In Section 2 the observations and pre-processing of the data is presented including merging of several observations and data reduction. In Section 3 I present the core analysis of the data and the results of the analysis. This includes analysing the spectrum, determining the angle of the cones/cross-cones, visual inspection, detailing the point spread function simulations which have been used as a model and analysing the resulting radial profiles. In Section 4 the FWHMs of the radial profiles are presented and discussed. Section 5 presents a discussion of the results of my findings and compares them to other literature on the subject. My conclusions are presented in Section 6.

2 OBSERVATIONS AND PRE-PROCESSING

2.1 Observations and Data Reduction

This work includes 2 archival observations and 4 recent observations of NGC 3393 taken with the *Chandra* X-Ray Observatory using the Advanced CCD Imaging Spectrometer (ACIS) instrument. Data were downloaded from the *Chandra* Data Archive¹ (PI:Maksym). The back-illuminated ACIS-S3 chip was used for all observations in this work. Table 1 lists the raw exposure time of each observation. The merged exposure time is 318.82 ks.

To reduce and analyse the data I used the *Chandra* Interactive Analysis of Observations (CIAO, Fruscione et al. 2006) 4.10 and the *Chandra* Calibration Database (CALDB) 4.8.0. For assistance in my analysis, I followed the CIAO threads².

The data were cleaned before analysis was carried out. The first step was reviewing the data in SAOImageDS9(DS9)³ to determine which ACIS chip the AGN was present on. For NGC 3393, all data was on the ACIS-S3 chip and therefore the event files for NGC 3393 were limited to the chip ACIS-S3 and to the energy range 0.3 keV - 8.0 keV, because this is the range that *Chandra's* ACIS-S detector is most effective over⁴.

Background flares are abnormally high count rates when a group of photons, which are not from the target source, enter the detector within a short interval, causing a spike in the count rate. Their removal improves the signal to noise of the data.

The process of removing background flares primarily involves limiting the count rate to $\pm n\sigma$ of the mean, where n is an integer. A region was created around the desired AGN and point sources in the frame and this region was excluded from a copy of the event file. This is so that any high count rate emission from the AGN and other point sources is not mistakenly removed. The second step was producing a light curve of the data by running the CIAO tool *dmlcextract* with bins of 200 seconds. Then *lc_sigma_clip* is run. This tool calculates the mean value of the count rate from the light curve for the event file. It then calculates the limits of $\pm n\sigma$ based upon the chosen value of n . Therefore any erroneous periods of low count rate are also removed alongside the background flares, removing all potential erroneous data. I decided that $n = 3$ would be sufficient. The output is set as a Good Time Interval(GTI) file. This GTI file is essentially a filter for the data, based upon the value of n specified. The original data was then filtered using this GTI file to remove the periods of high and low counts. The resultant exposure times are shown in Table 1. I wrote a script to automate this process for all observations.

As an example of this process, Figures 2 and 3 demonstrate a flare in the light curve of an observation and its removal. In Figure 2 a flare can be seen as a spike in the count rate displayed by the black points. Figure 3 shows

¹ <https://cda.harvard.edu/chaser/>

² <http://cxc.cfa.harvard.edu/ciao/threads/>

³ <http://ds9.si.edu/site/Home.html>

⁴ *Chandra* Proposers' Observatory Guide, Section 1.14, <http://cxc.cfa.harvard.edu/proposer/POG/html/chap1.html>

Table 1: Observation Log and Exposure Times

Obs ID ^a	Obs Date ^b	Counts ^c	Raw ET(ks) ^d	Processed ET(ks) ^e	Loss(%) ^f
21047	2018 Mar 23	2996	95.84	90.60	5.5
12290	2011 Mar 12	4348	69.16	67.19	2.8
20498	2018 Mar 18	1416	44.52	42.35	4.9
21048	2018 Jul 23	1279	40.43	38.82	4.0
20497	2018 Mar 19	1269	39.54	38.32	3.1
4868	2004 Feb 28	1921	29.33	23.80	18.9
Merged	...	13228	318.82	301.08	5.6

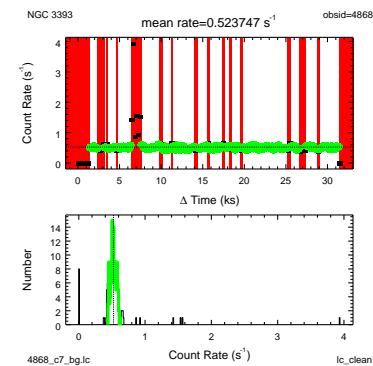
Notes.^a Chandra observation identification number.^b Date which the observation was taken.^c Number of counts enclosed within a 15'' circle centred on the nuclear source.^d Exposure time from the raw observations.^e Exposure time from the observations, after they have undergone background flare removal at a sigma level of $\pm 3\sigma$.^f Percentage of exposure time lost due to background flare removal.**Figure 2.** Top: Light curve for the observation 4868 of NGC 3393. The points in green are within the $\pm 3\sigma$ limit, therefore being allowed by the clipping program. Bottom: Histogram showing peaks in count rate of photons.

that the GTI file detects these high count rates so that they can be removed.

2.2 Merging

To obtain the best signal to noise ratio I merged the observations in Table 1.

The observations were initially merged using point sources in the field of view, excluding the focus of the study (NGC 3393), using a script which implements CIAO tools. First, the tool *fluximage* creates an exposure-corrected image for the event file, in a region which is approximately the size of the ACIS-S3 chip, 515'' x 515''. This image has a binning of 0.5 ACIS pixels, which allows us to look for small-scale structure. The tool *mknpsfmap* finds the PSF size for each pixel in the image at an energy of 2.3 keV and an encircled counts fraction of 0.9. This then allows for *wavdetect* to be applied to detect the point sources that are within the region. The result of *wavdetect*'s detections can be seen in Figure 6. The coordinate offsets between each of the same point sources in two different observations were then calculated. The coordinate system used for this work was the J2000 Celestial Coordinate System. The observations were

**Figure 3.** Top: Light curve for the observation 4868 of NGC 3393, showing a background flare and low count rates being highlighted in red by the GTI file, because they are outside the $\pm 3\sigma$ limits. Bottom: Histogram showing peaks in count rate of photons.

then shifted by this offset using *wcs_update*. The aspect solution files were shifted using the tool *reproject_aspect*. The observations were reprojected around the observation 12290 because this observation has the largest number of counts (see Table 1). Once all observations were reprojected, the data were merged using *merge_obs*.

The issue with this merge was that double features existed in point-like sources. In Figure 4 I show this in the nuclear source in the hard continuum and in Figure 7 it can be seen that this merge also failed in matching the point sources in the Fe-K α line. These features also existed in the broadband and in the most intense point sources. I know in the energy band depicted in Figure 4, 4.0 keV - 6.0 keV, I would expect a single prominent point source for the nuclear source (Fabbiano et al. 2019), which I do not see. Therefore, for the data analysis that was to be carried out, a more accurate merge was desired so that the emission could be investigated to the centre of the AGN.

To explore if I could produce a better merged image the AGN in the hard continuum was used as a reference, where there should only be one peak. I returned to the original cleaned data, which was unaffected by the previous method's reprojections because they were carried out on a copy of the

Table 2: Observation Shifts

Obs ID	X(Ra, ArcSec) ^a	Y(Dec, ArcSec) ^b
4868	-0.009	0.04
21047	0.245	-0.994
21048	0.011	-0.124
20497	0.095	-0.099
20498	-0.042	-0.009

Notes.

^a Ra shifts of the observation relative to the previous merge.
^b Dec shifts of the observation relative to the previous merge.

data. This is to allow different methods to be applied to the same data, to allow me to review which outcome is best for my scientific goal.

The centroid method involves two observations in DS9, overlaid in two different colours. Subpixel imaging involves using algorithms to improve the spatial resolution of the Chandra ACIS observations (Li et al. 2004). This allows us to resolve small scale structure by binning to smaller than one pixel. After binning to 1/16th ACIS pixels and to the hard continuum, 4.0 keV - 6.0 keV, the colourbar is adjusted until only the most luminous central region (<0.1'') is visible; it is this point which the observations are merged with respect to. Here I have limited the hard continuum to between 4.0 keV and 6.0 keV because there is a small possibility of soft X-ray photons around 3.0 keV. This shall be verified with a spectrum later on in this work.

A box region was used to determine the X(Ra) and Y(Dec) distance between the two central points. These distances are measured in arcseconds. To convert them to native ACIS pixels, a division by the pixel size is required; 0.492'' for ACIS. These shifts are noted in Table 2.

The event file was then updated with these astrometric shifts using *wcs_update* and the aspect solution file reprojected using *reproject_aspect*. To update the header of the corrected event file with the corrected aspect solution file, *dmhedit* was used. This shifted observation is then merged with the astrometric reference observation, Obs ID 12290, using *merge_obs*. This produces a merge of two observations, denoted merged_1. This process is repeated for the next observation, using merged_1 as the astrometric reference and once the shifts are obtained manually, I automated the remaining steps.

One may think that Obs ID 12290 could be used as the astrometric reference for all of the shifts that are required. However, the shifts must be accurate to within 0.2'' for the best chance at getting only one peak. Therefore for 6 observations where the central points have a 0.1'' error, if they were all merged on the same astrometric reference some points could be on either side of the central point and be more than 0.2'' apart. This would not be a good enough merge because I am analysing the emission from the central and outer regions. Therefore the remaining observations are merged using the latest merged file each time as the new astrometric reference. The merged files are visually inspected after each merge to check for double features.

To check that this centroid merging technique had reduced the number of peaks in the hard continuum and Fe-K α energy bands, the two merges are compared. Figure 4 shows this comparison in the hard band where the merge using the point sources has multiple peaks and the merge using the

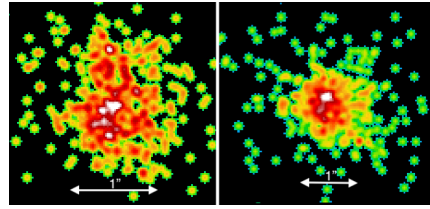


Figure 4. The nucleus of NGC 3393. Both images are in the energy band 4.0 keV - 6.0 keV and have been Gaussian smoothed using a radius of 3, a sigma of 1.5 and is at a binning of 1/16th native ACIS pixel. Further binning was required to distinguish clear multiple peaks beyond a binning of 1/8th native ACIS pixels. Left: Image of the merge carried out using the point source matching technique. Right: Image of the merge carried out using the centroid matching technique.

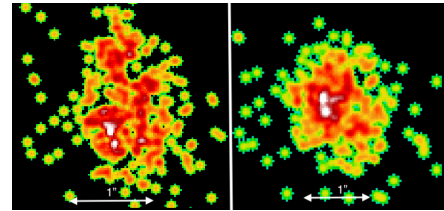


Figure 5. The nucleus of NGC 3393. Both images are in the energy band 6.1 keV - 6.6 keV and have been Gaussian smoothed using a radius of 3, a sigma of 1.5 and is at a binning of 1/16th native ACIS pixel. Further binning was required to distinguish clear multiple peaks beyond a binning of 1/8th native ACIS pixels. Left: Image of the merge carried out using the point source matching technique. Right: Image of the merge carried out using the centroid matching technique.

centroids has one or two. In Figure 5 the Fe-K α band is depicted. It shows that in the merge using point sources there are more separate sources. In both figures, it can be seen that the centroid merge is more similar to a point spread function around a central point, which I would expect to see.

I can see from Figures 7 and 8 that the point sources in the merge using centroiding have fewer peaks and take the shape more of a point spread function than the point sources in the merge which used point sources. For bright (surface brightness > 5 counts/arcsec²) point sources within 100'' radius of the AGN, the merge is successful with no double features appearing at a binning of 1/8th native ACIS pixels.

In Figure 9 I show one observation and in Figure 10 I show the merge of 6 observations. It can be seen that the extent of the cone regions is much clearer in the merge. Here the cone regions are defined as those in the NE and SW regions, with the cross-cone regions in the NW and SE regions. The statistics for the cone and cross-cone regions in Figure 9 looks weak and in areas, it is similar to the background. As can be seen from Table 1, these statistics are greatly improved upon in Figure 10, allowing me to have greater confidence in any results I obtain.

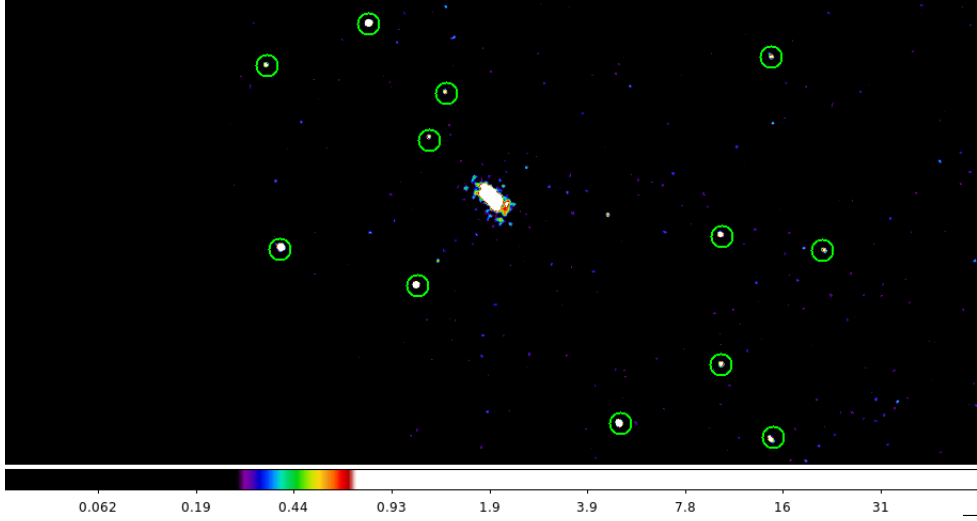


Figure 6. Wavdetect field of Obs ID 21047 showing the point sources detected in the energy band 0.3 keV - 8.0 keV. Region is approximately $500'' \times 240''$ and has been Gaussian smoothed using a radius of 3 and a sigma of 1.5.

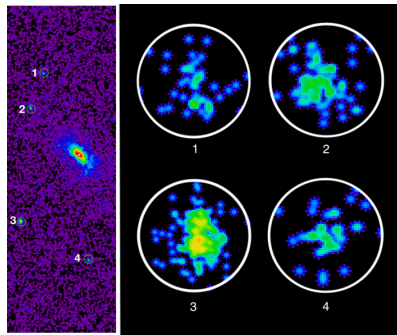


Figure 7. Left: Location of point sources depicted in the wavdetect field from Figure 6. Right: Point sources in the energy range 0.3 keV - 8.0 keV from the merge using point sources at 1/8th ACIS pixel, Gaussian smoothed using a radius of 3 and a sigma of 1.5. The approximate radius of each circle is $1.7''$. Distance to the furthest out point source from the centre is $\sim 63''$.

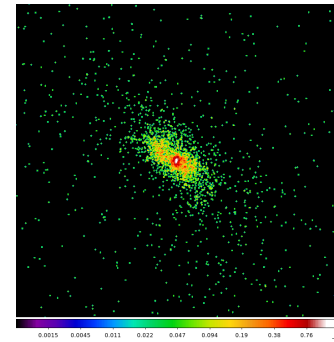


Figure 9. Gaussian smoothed image of Obs ID 21047 of NGC 3393 in the energy band 0.3 keV - 8.0 keV using a radius of 3 and a sigma of 1.5

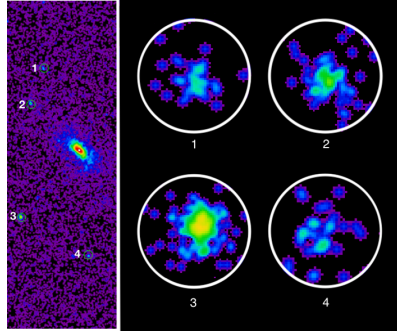


Figure 8. Left: Location of point sources depicted in the Wavdetect field from Figure 6. Right: Point sources in the energy range 0.3 keV - 8.0 keV from the merge using centroiding at 1/8th ACIS pixel, Gaussian smoothed using a radius of 3 and a sigma of 1.5. The approximate radius of each circle is $1.7''$. Distance to the furthest out point source from the centre is $\sim 63''$.

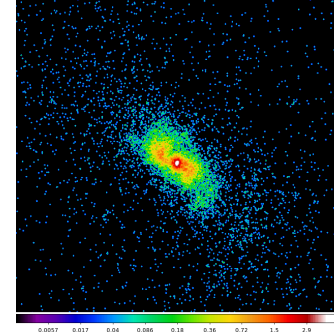


Figure 10. Gaussian smoothed image of the merge of 6 observations of NGC 3393 in the energy band 0.3 keV - 8.0 keV using a radius of 3 and a sigma of 1.5

3 ANALYSIS

3.1 Spectrum

Figure 11 shows the observed ACIS-S spectrum of NGC 3393. The CIAO tool used to produce the spectrum was *specextract*. The background has been subtracted and the spectrum spans the range 0.3 keV - 8.0 keV, with 10 counts per bin. The different energy bands that are being investigated are shown in Figure 11 by the colour shaded areas. The area shaded in yellow is the soft band, between 0.3 keV and 3.0 keV, which has been spatially extended corresponding to the optical emission line 'cone' (Maksym et al. 2017).

The area shaded in turquoise is the hard band from 3.0 keV - 6.0 keV with the range 4.0 keV - 6.0 keV being the hard continuum. The area shaded in purple is the Fe-K α band, between 6.1 keV - 6.6 keV. In this region there is a clear peak at \sim 6.4 keV due to Fe-K α . These features are the reason these energy bands have been investigated.

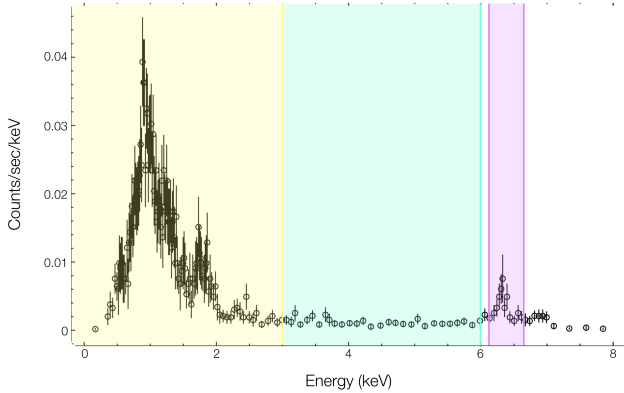


Figure 11. Observed spectrum of NGC 3393 from Obs ID 21047 between 0.3 keV - 8.0 keV using a 12'' radius centred on the AGN, after background subtraction.

3.2 Cones

The majority of radiation emitted in the X-ray by NGC 3393 is through two ionisation cones, in the NE and SW (see Figure 10). Radiation is emitted isotropically from the accretion disk and but due to the shape of the torus, it is confined to the torus' opening. In these cone regions lie clouds, either from the ISM or from winds originating from the accretion disk. Photoionisation by the AGN radiation of these clouds results in stimulated emission, with some of that emission oriented towards the telescope, which approximately presents in the shape of two cones.

The angles of the cone have been deduced using azimuthal binning of an annulus, centred on the hard continuum peak, extending out to 15''. The central 0.3'' has been excluded and all point sources have been removed within a 100'' radius of the centre. The annulus was then split up into 1 degree bins and the counts in each bin were summed. The result can be seen in Figure 12. The troughs have been fitted using an equation of the form $\text{Counts} = A \sin(2(\text{Angle}) + C) + D$ where A is amplitude, C is the phase and D is the Counts intercept of the sine function.

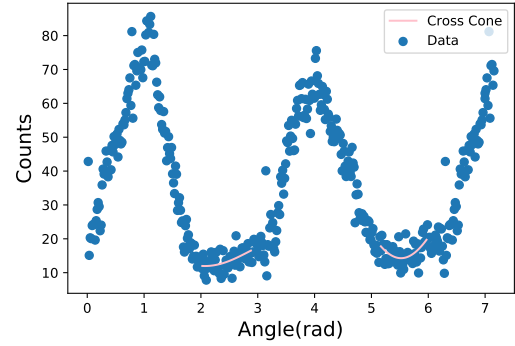


Figure 12. Azimuthal profile centred on the hard continuum, 4.0 keV - 6.0 keV. Angles measured from the north.

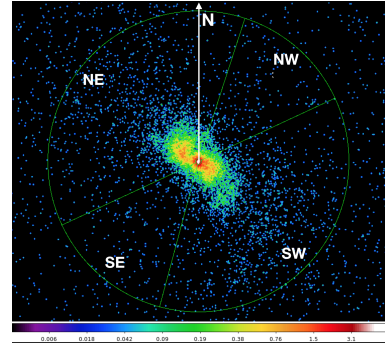


Figure 13. Cone and cross-cone regions depicted within a circle with a 15'' radius. The energy band of this image is 0.3 keV - 8.0 keV and it has been Gaussian smoothed using a radius of 3 and a sigma of 1.5.

tion. The troughs have been fitted conservatively. This is because I want to be confident that any results I obtain for the cross-cone region have actually originated from the cross-cone region and not the fringes of the cones.

The NE Cone is at $48.5^\circ \pm 66.5^\circ$ and the SW Cone is $230^\circ \pm 65^\circ$. The SE cross-cone is $138.5^\circ \pm 25^\circ$ and the NW cross-cone is $320^\circ \pm 23.5^\circ$. All angles are measured counter-clockwise from the north. These cones can be seen in Figure 13.

3.3 Images

The images as seen in Figure 14 were produced across various energy bands after binning to $1/8^{\text{th}}$ native ACIS pixel. They were all adaptively smoothed using CIAO 4.10 with the settings of kernel radii from 1'' to 25'', 10 counts under kernel, 30 iterations and the spacing between radii is logarithmic. If there were no extent then the images would look identical to an image of Chandra's Point Source Function (PSF), which is approximately a circle. Therefore in Figure 14a, I can see that it is in the soft band, 0.3 keV - 1.5 keV, that this extent is most prominent, especially in the NE and SW cones. The NW cross-cone also shows clear extent. Figures 14b and 14c also show this extent in the cone in the 1.5 keV - 3.0 keV energy band and the 3.0 keV - 4.0 keV energy band. In Figure 14d I can see that in the 4.0 keV

- 5.0 keV energy band there is clear extent in the NE cone and the possibility of extent in the SW cone. There seems to be little extent in the cross-cone. In Figure 14e there is little extent in both cone and cross-cone. However, there does seem to be some extent in the wider regions of the cone regions and in the SE cross-cone region. In Figure 14f there is no extent in the cross-cone regions. In the cone regions there is a small amount of extent, in a more north/south direction tilted slightly towards the cone regions. Therefore in the hard band (3.0 keV - 6.0 keV), there is visual extent. These results will be confirmed with the radial profiles.

3.4 PSF Simulations

Visually there seems to be extended emission when looking at the broadband and hard band images of NGC 3393. To quantify this extended emission I need to compare it to a model of the Chandra Point Source Function (PSF). To model the PSF I used the Chandra Point Source Function simulation⁵. If the radiation originated only from the AGN's accretion disk and torus, I would expect point-like emission. By taking the radial profiles of the PSF simulation and the AGN I am able to quantifiably determine the extent of the emission from NGC 3393. If the source (NGC 3393) is off-axis when being observed with the Chandra X-ray telescope, then distortion of the image is possible. This distortion could be mistaken for extended emission and therefore this extended emission could be a red herring. The PSF simulation should also depict this distortion if this were to be the case.

The first step in generating the PSF simulations is gathering the required information to input into the Chandra Ray Tracer(ChaRT). ChaRT simulates rays of photons travelling through Chandra's optical setup, at a specified monochromatic energy, to produce a collection of rays at a specified aimpoint. The MARX⁶ program then allows for these rays to be projected onto the detector to produce fits files. These fits files can then be merged to create an event file, which is comparable to the merged event file of the observations. The simulations are produced for each different energy band being investigated.

The inputs that ChaRT requires are the R.A. and Dec. coordinates of the source, the source spectrum, pointing information and the number of iterations. The source coordinates were obtained by creating a circular region, centred on the central region of the AGN for each different energy band and taking the central coordinates of this circle. All simulations were based upon a monochromatic energy and this energy was the midpoint between the upper and lower limit of the current energy band. The photon flux, which is the number of photons per cm² per second, was calculated using a CIAO tool named *srcflux*. The necessary pointing information for the ray tracer is found in the aspect solution file for each observation, so this is provided. The number of iterations was set to 50 because this is the highest number of iterations the ray tracer allows for and the highest statistics model possible will produce the most accurate shape of the PSF.

The MARX parameters then need to be set. The SIM

Offset is the x, y, and z distance that the science instrument module is away from its original position. Therefore this is calculated from its current (at the time the observations were taken) and original positions. The nominal values for the R.A., Dec. and Roll are in the header of the event file. The aspect blur is set to 0.25, an appropriate value for the ACIS-S detector⁷. Chandra follows a Lissajous pattern when observing which allows sub-pixel analysis of the data. In order to replicate this in the simulation, the dither file is set to the aspect solution file of the observation in question. The exposure time is set to 0.0.

The rays are then projected using MARX and a fits file of the result is created. This happens for all 50 ray files. The multiple simulations are then combined using *dmmerge* to create a final fits image that can be compared with the data after normalisation.

3.5 Radial Profiles

In order to compare the data to the simulations, I produced radial profiles of both the observation and the simulation. After binning to 1/8th native ACIS pixel, elliptical panda regions were created to obtain the radial profile in DS9. This allows for many annuli to be created, for each different cone/cross-cone region. The angles of the cones are chosen as described in Section 3.2. The radial bins increase in size as you move away from the centre of the AGN to obtain higher statistics for the larger radii where there are typically fewer counts. The radius is taken as the midpoint of the radial range for a given bin. DS9 is used to calculate the surface brightness within each radial region and displays it as a table of data, where the surface brightness is calculated as

$$\text{brightness}_s = \frac{\text{counts}}{\text{area}} \quad (2)$$

where 'counts' is the sum of counts within the smaller region and 'area' is the area of that region, in arc seconds squared. Since the error on the area is assumed to be zero, the error on the surface brightness, error_b , is given by

$$\text{error}_b = \frac{\text{error}_c \times \text{brightness}_s}{\text{counts}} \quad (3)$$

where error_c is the error in the counts, given by the shot noise, $\sqrt{\text{counts}}$.

Once this has been completed on the data and the central region, which is a circle of 0.3'' in radius centred on the centre of the AGN, it is repeated on the PSF simulation, with the exact same regions. The surface brightness of this central region is used as the normalisation point between the observational data and the simulation and its radial midpoint is fixed at 0. I wrote a script to automate the PSF simulation and radial profile data retrieval for each energy band.

The simulation is normalised using a normalisation factor, given by

$$\text{Normalisation Factor} = \frac{\text{brightness}_{s,\text{psf},\text{center}}}{\text{brightness}_{s,\text{obs},\text{center}}} \quad (4)$$

⁵ <http://cxc.harvard.edu/ciao/PSFs/chart2/>

⁶ <https://space.mit.edu/CXC/MARX/>

⁷ <http://cxc.harvard.edu/ciao/why/aspectblur.html>

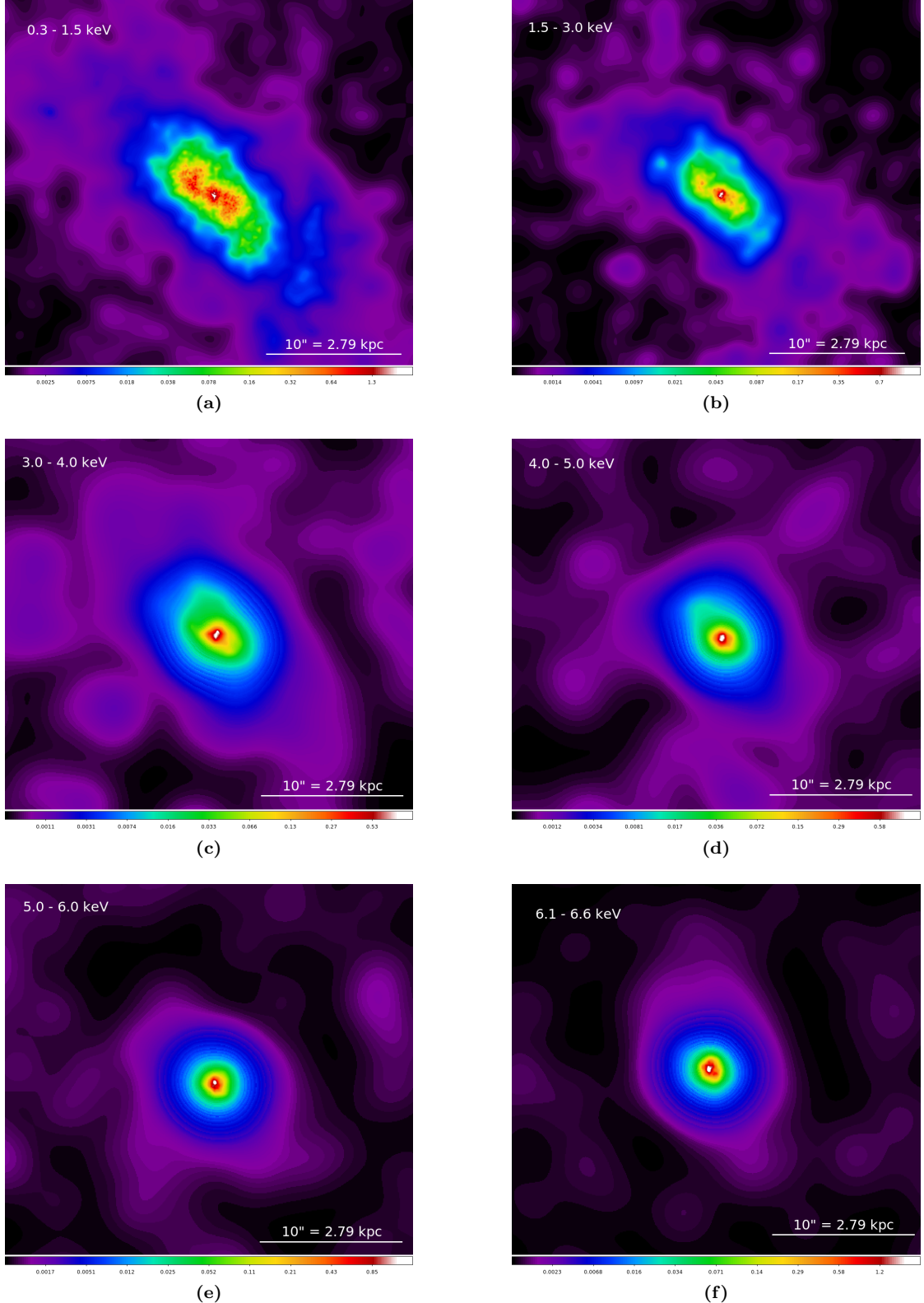


Figure 14. Adaptively Gaussian smoothed observations of NGC 3393 which have been binned to $1/8^{\text{th}}$ native ACIS pixels. All images have kernel radii from 1 to 25, 10 counts under kernel, 30 iterations and the spacing between radii is logarithmic. (a) is 0.3 keV - 1.5 keV, (b) is 1.5 keV - 3.0 keV, (c) is 3.0 keV - 4.0 keV, (d) is 4.0 keV - 5.0 keV, (e) is 5.0 keV - 6.0 keV, (f) is 6.1 keV - 6.6 keV.

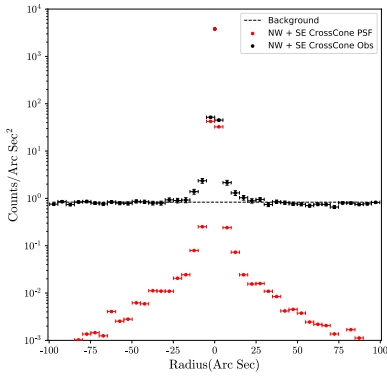


Figure 15. Radial profile of NGC 3393 extending out to $100''$ in the NW and SE cross-cone directions.

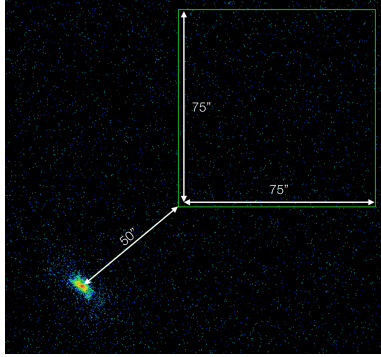


Figure 16. Dimensions of background region and distance from centre of NGC 3393.

where $\text{brightness}_{\text{s,psf,center}}$ and $\text{brightness}_{\text{s,obs,center}}$ are the surface brightness' from their respective central regions.

The central and elliptical panda regions in all energy bands are centred on the hard continuum, which from the spectrum is between 4.0 keV - 6.0 keV.

Figure 15 shows the radial profile of the 0.3 keV - 8.0 keV energy band, out to a radius of $100''$, for the observational data (in black) and the normalised PSF (in red). I notice that the source profile flattens at large radii. This is because it reaches the surface brightness values of the field background. Within this region point sources have been removed because they will affect the background reading. They are also not in any of the future radial profiles.

From Figure 15 it can be seen that at $>50''$ the surface brightness is equal to the background. Therefore the background region should be at least $50''$ away from the centre of the AGN, in the cross-cone region. It has been taken in the cross-cone regions because there are fewer counts in this direction. Therefore, an accurate background region is less distance away and can be larger when compared with a background region in the cone direction. This is important because the chip has a limited size and the larger the background region, the more accurate the measurement. The largest region in this distance away from the centre and within the ACIS-S3 chip was $75'' \times 75''$. There are no point sources in this region and so this is an accurate reading. This can be seen in Figure 16.

The background, taken from the observation, is then

subtracted from the data. The radial profiles are then plotted, as surface brightness against radius.

Figure 17 depicts the radial profiles over the energy bands: 0.3 keV - 1.5 keV, 1.5 keV - 3.0 keV, 3.0 keV - 4.0 keV, 4.0 keV - 5.0 keV, 5.0 keV - 6.0 keV and 6.1 keV - 6.6 keV. For each energy band the radial profile has been taken in the cone and cross-cone direction. The radial profile of the observation is shown in black and the radial profile of the PSF simulation is shown in red.

From Figures 17a and 17b it can be seen that the cone and cross-cone profiles in the energy band 0.3 keV - 1.5 keV are both extended. Each SW and NE cone in Figure 17a is extended to $\sim 27.5''$ (~ 7.7 kpc) and in total the cone regions are extended to $\sim 55''$ (~ 15.3 kpc). In Figure 17b it can be seen that the NW and SE cross-cones are extended to $\sim 27.5''$ (~ 7.7 kpc) each and $\sim 55.0''$ (~ 15.3 kpc) together. Although there are a few regions at $\sim 8-9''$ where the observational data is consistent with the PSF.

From Figures 17c and 17d the cone and cross-cone regions of NGC 3393 in the energy band 1.5 keV - 3.0 keV are also extended. In Figure 17c I can see that each SW and NE cone is extended in the region $\sim 1.0''$ to $\sim 15''$ (~ 0.3 kpc to ~ 4.2 kpc) and in total the cone regions are extended by $\sim 28''$ (~ 7.8 kpc) between $\sim 1.0''$ to $\sim 15''$. From Figure 17d it can be seen that the NW cross-cone is extended between $\sim 1.0''$ to $\sim 3.0''$ (~ 0.3 kpc to ~ 0.8 kpc). Beyond this there is some extent out to $\sim 12''$ (~ 3.3 kpc) but some regions are consistent with the PSF. The SE cross-cone is also extended in the region $\sim 1.0''$ to $\sim 3.0''$ (~ 0.3 kpc to ~ 0.8 kpc) at low radii and is extended between $\sim 9.0''$ and $\sim 15''$ (~ 2.5 kpc to ~ 4.2 kpc) in the wing. Together the cross-cone is extended by at least $\sim 2.0''$ (~ 0.6 kpc) in the region $\sim 1.0''$ to $\sim 3.0''$.

From Figure 17e the cone regions are extended in the energy band 3.0 keV - 4.0 keV. The SW and NE cone regions are both extended in the region $\sim 1.0''$ to $\sim 16.0''$ (~ 0.3 kpc to ~ 4.5 kpc) and in total by $\sim 15''$ (~ 4.2 kpc) beyond $\sim 1.0''$ to $\sim 16.0''$. From Figure 17f it can be seen that in general the 3.0 keV - 4.0 keV cross-cone is consistent with the PSF but it is extended in the SE direction at radii between $\sim 6.0''$ to $\sim 16.0''$ (~ 1.7 kpc to ~ 4.5 kpc).

From Figure 18a the cone region is extended in the energy band 4.0 keV - 5.0 keV. In the SW direction there is extent in the region $\sim 2.0''$ to $\sim 15.0''$ (~ 0.6 kpc to ~ 4.2 kpc). In the NE direction there is extent around the region near $\sim 5''$ and the region near $\sim 20''$ but in general, it is consistent with the PSF. In Figure 18b the cross-cone is not extended in the energy band 4.0 keV - 5.0 keV.

From Figure 18c it can be seen that the cone region in the energy band 5.0 keV - 6.0 keV is mostly consistent with the PSF. There is extent around the region near a radius of $\sim 4.0''$ (~ 1.1 kpc) in the SW direction and between $\sim 5.0''$ and $\sim 15.0''$ (~ 1.4 kpc and ~ 4.2 kpc) in the NE direction. The cross-cone regions in Figure 18d only show an extended region between $\sim 5.0''$ and $\sim 15.0''$ (~ 1.4 kpc and ~ 4.2 kpc) in the SE direction.

From Figure 18e it can be seen that the cone region in the energy band 6.1 keV - 6.6 keV is extended only in the NE direction between $\sim 2.0''$ and $\sim 18.0''$ (~ 0.6 kpc and ~ 5.0 kpc). From Figure 18f it can be seen that the cross-cone regions are not extended except possible extent between $\sim 12.0''$ and $\sim 18.0''$ (~ 3.3 kpc and ~ 5.0 kpc).

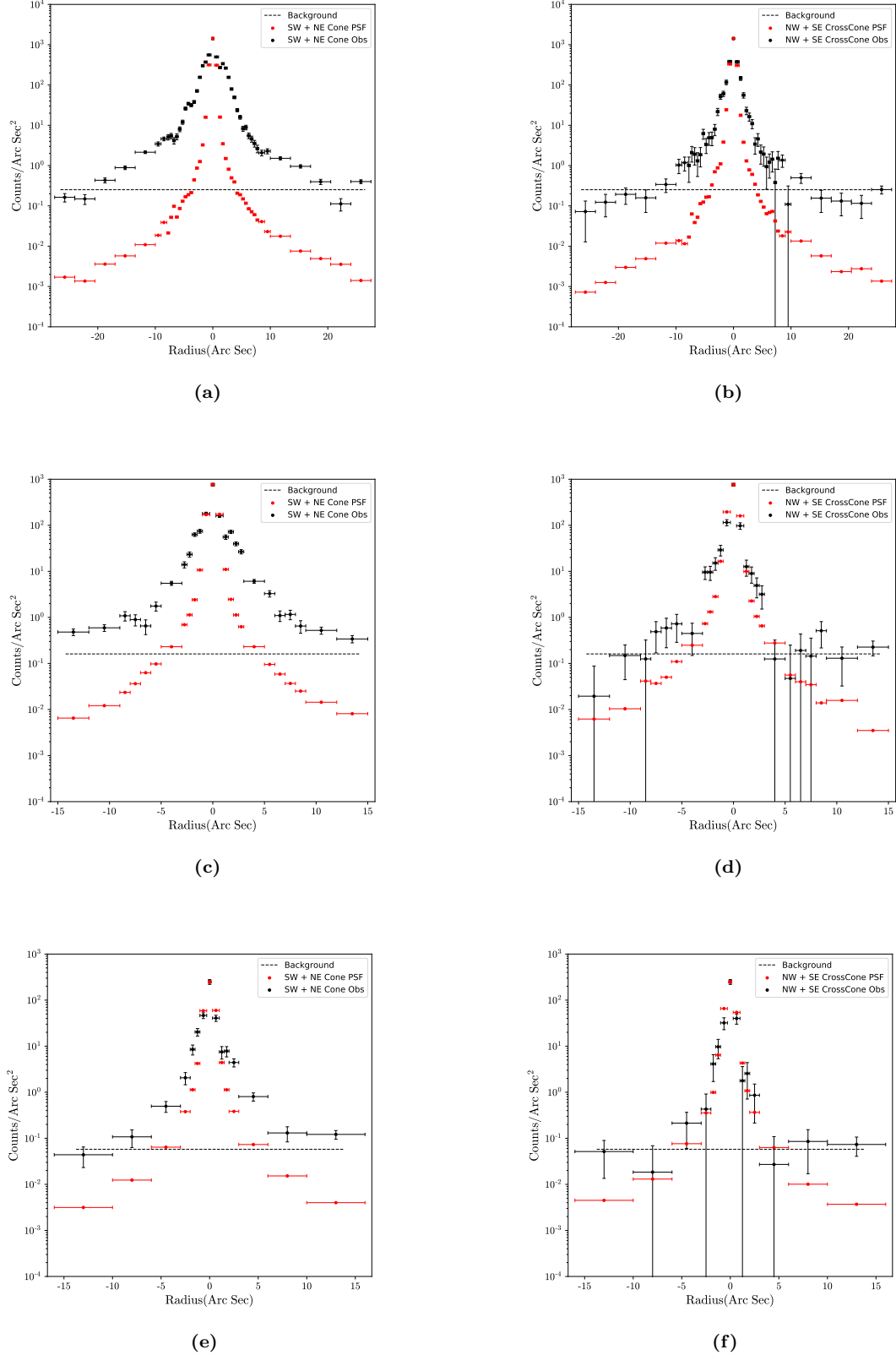


Figure 17. Surface brightness radial profiles of the observational data (in black) compared to the Chandra PSF simulation (in red). (a) is the cone, 0.3 keV - 1.5 keV, (b) is the cross-cone, 0.3 keV - 1.5 keV, (c) is the cone, 1.5 keV - 3.0 keV, (d) is the cross-cone, 1.5 keV - 3.0 keV, (e) is the cone, 3.0 keV - 4.0 keV, (f) is the cross-cone, 3.0 keV - 4.0 keV.

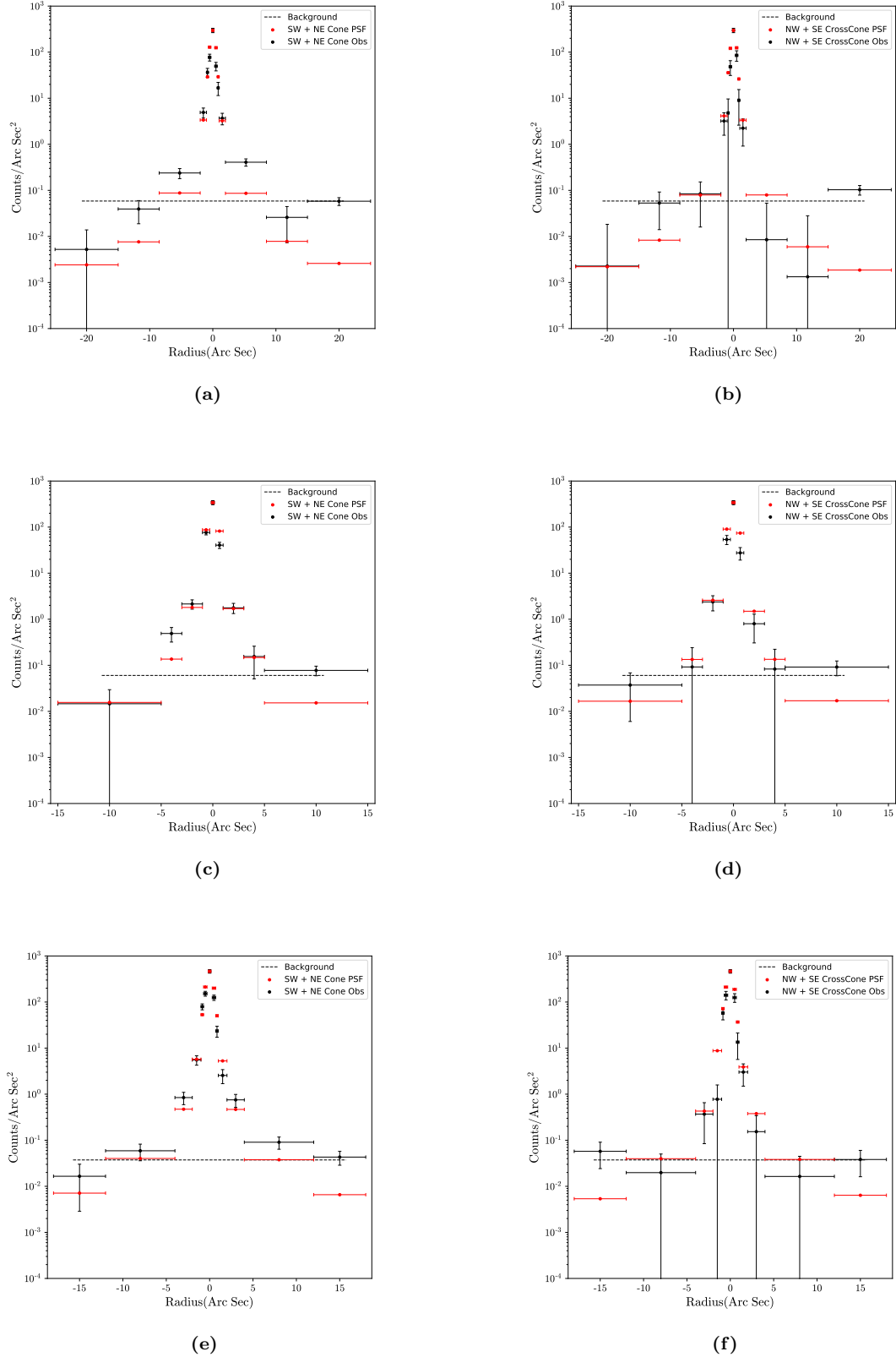


Figure 18. Surface brightness radial profiles of the observational data (in black) compared to the Chandra PSF simulation (in red). (a) is the cone, 4.0 keV - 5.0 keV, (b) is the cross-cone, 4.0 keV - 5.0 keV, (c) is the cone, 5.0 keV - 6.0 keV, (d) is the cross-cone, 5.0 keV - 6.0 keV, (e) is the cone, 6.1 keV - 6.6 keV, (f) is the cross-cone, 6.1 keV - 6.6 keV.

4 PROFILE WIDTH VS. ENERGY

To examine the trend in the extent of the emission as a function of the energy, the FWHM of the radial profile intensity was measured. This trend is investigated in the \log_{10} of the cone and cross-cone regions. The logged data is then randomised using a Gaussian distribution and to within the error bars, correct to 1σ . Since the radial profiles account for bi-cones, there is data in what I have defined as the positive radial direction and data in the negative radial direction. This is split. In the positive direction, a Monte Carlo simulation is set up to estimate the HWHM on the positive side, repeating 10,000 times; 5000 for the upper errors and 5000 for the lower errors. The logarithm of this data is $\log_{10}(\text{data})$ and the upper and lower error bars are given as $\log_{10}(\text{data} + \text{upper error}/\text{data})$ and $\log_{10}(\text{data} - \text{upper error}/\text{data})$ respectively. Occasionally after background subtraction has taken place the data value will be less than the error value. This is especially common at larger radii, where the data value nears the background value. If this is the case, the equation for evaluating the lower errors in logarithmic form cannot be carried out, due to the logarithm of a negative number being undefined. In these cases, the lower error is set to 0 and a value for the data point is chosen from a uniform random distribution, between zero and the data value. A spline interpolation is then fit to each piece of the randomised data. The HWHM is then calculated based upon this spline equation. The resulting HWHM is the median from the 10,000 iterations. The index of the upper error boundary is then taken as the median + 34% of 10,000 (half of 1σ , because this value is the HWHM error). The error is then calculated as this value of the HWHM at this value subtract the median HWHM value. The lower error boundary is taken in a similar procedure, except the lower error boundary index is 34% below the median and it is calculated as the median subtract the value of the HWHM at the lower error boundary. This calculation works out the HWHM, half of the FWHM, and this is why the 1σ error (68%) has been split in two. An equivalent process is applied to the surface brightness profile for negative radii. The HWHMs for the positive and negative sections are then added to produce a FWHM. This procedure is applied separately to the cone and the cross-cone directions. The errors are propagated using

$$\text{upper error} = \sqrt{(\text{upper error}_{+\text{ve}})^2 + (\text{upper error}_{-\text{ve}})^2} . \quad (5)$$

An equivalent method is applied to the lower errors. Only values that are larger than the FWHM of the PSF, and therefore only those which show extended emission, are plotted. The size of the PSF FWHM is $\sim 2''$ (~ 0.6 kpc). The values of FWHM are plotted versus energy in Figure 19.

The full width is also evaluated at the value of 3 dex below the maximum value of surface brightness and this shall be denoted FW3dex henceforth. The use of the FW3dex is to investigate the extended emission in regions of larger radii, away from the central source. The FW3dex of the PSF profile is $\sim 4''$ (~ 1.1 kpc).

From Figure 19 it can be seen that at half the maximum surface brightness the cone is extended between the 0.3 keV - 1.5 keV and 4.0 keV - 5.0 keV energy bands, with FWHMs of $\sim 7.2''$ (~ 2.0 kpc) and $\sim 1.9''$ (~ 0.5 kpc) respectively. The cross-cone is extended between the 0.3 keV - 1.5 keV and 1.5

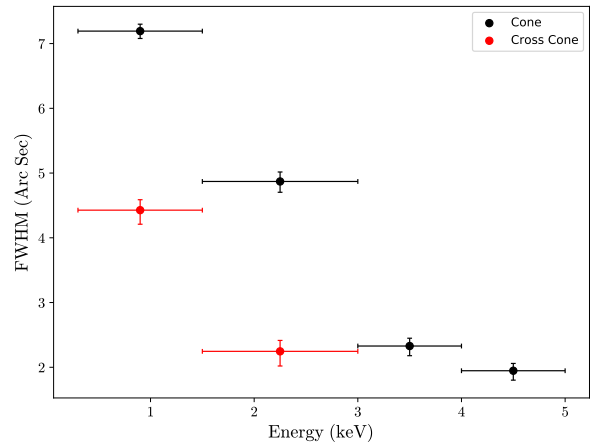


Figure 19. FWHM of cone and cross-cone in NGC 3393. Errors are 1σ .

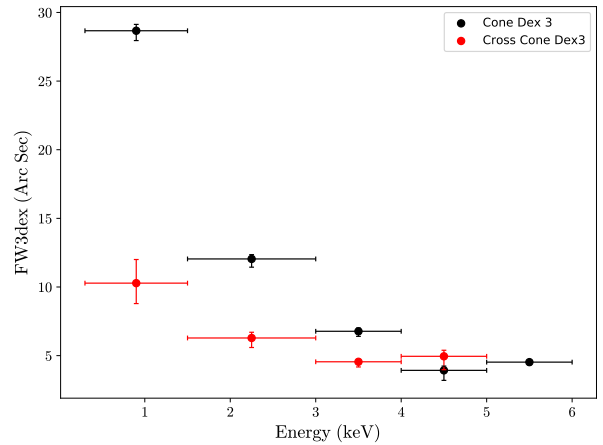


Figure 20. Full width at 3 dex below maximum surface brightness of the cone and cross-cone in NGC3393. Errors are 1σ .

keV - 3.0 keV energy bands, with FWHMs of $\sim 4.4''$ (~ 1.2 kpc) and $\sim 2.2''$ (~ 0.6 kpc) respectively. In both the cone and cross-cone regions the FWHM decreases with increasing energy. The cone is extended in the lower hard band (3.0 keV - 5.0 keV). The cross-cone is not extended in the same band. Neither the cone or cross-cone is extended in the spectral band which contains the iron line, at ~ 6.4 keV and therefore neither FWHMs have been plotted for these profiles. There is a consistent difference ($\sim 2.8''$) between the cone and cross-cone, although there are only two comparable energy bands.

Figure 20 shows the FW3dex. At this level, the cone and cross-cone are more extended than at the half maximum level. The cone is extended between the 0.3 keV - 1.5 keV and 5.0 keV - 6.0 keV energy bands, with the full widths being $\sim 28.6''$ (~ 8.0 kpc) and $\sim 4.5''$ (~ 1.3 kpc) respectively. The cross-cone is extended between the 0.3 keV - 1.5 keV

and 4.0 keV - 5.0 keV energy bands, with full widths of $\sim 10.3''$ (~ 2.9 kpc) and $\sim 5.0''$ (~ 1.4 kpc) respectively. The general trend for both the cone and cross-cone's full width is that they decrease as the energy increases. The size of the full width of the cross-cone is significantly less than that of the cone. Both cone and cross-cone show decreasing trends with increasing energy, although the gradient of the cross-cone decreases more slowly than the cone from a ratio of $\sim 1/3$ cross-cone to cone to equal, within errors.

5 DISCUSSION

In this section, I discuss the results of the images and radial profiles and what physical processes could explain them. I first discuss the extended soft band emission (Section 5.1) and then focus on the extended hard band emission (Section 5.2). The FWHM and FW3dex trends are then discussed (Section 5.3) and finally the transmission of the torus is discussed (Section 5.4).

5.1 Extended Soft Band Emission

The images of NGC 3393 show clear extended emission in the soft band (0.3 keV - 3.0 keV) (see Figures 14a, 14b) in both the cone and cross-cone regions. In Figures 17a-d this is supported by radial profiles of the observed surface brightness compared with the surface brightness radial profiles of the Chandra PSF. Figure 19 shows that at half maximum of the surface brightness, the soft cone and cross-cone regions are extended. They are also extended at a value of 3 dex below the maximum surface brightness (see Figure 20). This agrees with [Levenson et al. \(2006\)](#) who discovered extended emission in the X-ray soft band of NGC 3393. It is likely that this cone emission photoionises the narrow line region which extends out to many hundreds of parsecs. The free electrons recombine with other ions and the electron drops down a few energy levels. In the process it emits X-ray photons. This material in the narrow line region is likely due to accretion disk winds or ISM clouds. It is also possible that there is line emission from X-ray thermal emission. This can be produced when the radio jet collides with these dense photoionised ISM clouds causing the thermal emission. Due to the radio jet having a magnetic field, there is also a possibility of magnetically accelerated electrons emitting Synchrotron radiation at X-ray energies.

The presence of extended cross-cone emission may suggest that photons could have either escaped through the torus via areas of lower column density and then scattered in ISM clouds beyond the torus. However, this cross-cone extent may also be related to the interaction of the radio jet with dense ISM clouds, as suggested by the simulation of [Mukherjee et al. \(2018\)](#). The result of the simulation involves the presence of hot X-ray bubbles in the cross-cone region, which are then scattered towards our line of sight.

From Table 3 it can be seen that the count ratio of cross-cone to cone in the 0.3 keV - 1.5 keV energy band is over 2 times larger than the 1.5 keV - 3.0 keV energy band. In the Seyfert Type II CT AGN ESO 428-G014, a similar trend was seen, where the 0.3 keV - 1.5 keV energy band was ~ 1.7 times larger than the 1.5 keV - 3.0 keV energy band

([Fabbiano et al. 2018](#)). The reasoning for this in ESO 428-G014 was for an additional soft emission component, not due to the AGN with the possibility that this is hot ISM trapped in the potential of the galaxy ([Fabbiano et al. 2018](#) from [David et al. 2006](#)).

5.2 Extended Hard Band Emission

I also find extended emission in the hard band (3.0 keV - 6.0 keV). As the energy increases, the images show extent of the emission, as can be seen in Figures 14c to 14f. It can be seen from Figures 17e-f and Figures 18a-d that the radial profiles show extended kpc scale emission in the wings of the cones between 3.0 keV and 6.0 keV. For the cross-cone only in the wings are the profiles extended in this energy band. At half the maximum surface brightness the cross-cone region is not extended in the hard band, at any energy above 3.0 keV. However, the cone is extended up to 5.0 keV. At 3 dex below the maximum surface brightness, the cross-cone is extended up to 5.0 keV and the cone is extended up to 6.0 keV. The Fe-K α line is not extended in the cone or cross-cone at any value below the maximum of the surface brightness.

The cone emission in the hard band is not extended near the nuclear source, below $1''$ (~ 280 pc) however at radii larger than this, the cone is extended at some energies. In the 3.0 keV - 4.0 keV energy band, it is extended out to $\sim 16''$ (~ 4.5 kpc). This extent is evidence of there being sufficiently optically thick clouds close, ≥ 279 pc, to the SMBH and AD, in the molecular disk. Hard X-ray extent is unexpected according to the current model of CT AGNs ([Netzer 2015](#)) but similar was seen in the Seyfert Type II CT AGN ESO 428-G014 ([Fabbiano et al. 2017](#)). The kpc extent of the emission in the cone also suggests that these dense clouds are dispersed throughout the structure of the AGN, up to at least distances of ~ 4.5 kpc. This result shows that the result of Fabbiano et al. is not an isolated case. Both galaxies, ESO 428-G014 and NGC 3393, are spiral galaxies which therefore makes the presence of molecular clouds likely and could be why we see this extended hard emission in both. While the cross-cone direction is only extended in select energy bands and radii in the hard band, it is likely due to similar reasons of that in the soft band. These are a torus with varying column densities and the interaction between the radio jet and the molecular disk of the galaxy causing hot X-ray bubbles in the direction of the cross-cone ([Mukherjee et al. 2018](#)).

It can be seen from Table 3 that the extended observed luminosity in the hard band (3.0 keV - 6.0 keV) is $\sim 2.6 \times 10^{39}$ erg s $^{-1}$. This luminosity has been calculated with an unobscured flux calculated from PIMMS v4.9⁸ and then using the equation $L = \text{Flux} \times 4\pi D^2$ where D is the distance to the galaxy, ~ 53 Mpc. The PIMMS software calculates the flux by creating an energy spectrum and fitting it with a power law. This power law is given by

$$\text{Flux} = AE^{-\gamma} \quad (6)$$

where A is the normalisation term with units given by

$$A = \frac{\text{photons}}{\text{seconds} \times \text{keV} \times \text{cm}^2} \quad (7)$$

⁸ <http://cxc.harvard.edu/toolkit/pimms.jsp>

Table 3: Cross-Cone/Cone Count Ratios and Luminosity

Energy Band (keV)	0.3 - 1.5	1.5 - 3.0	3.0 - 6.0	3.0 - 4.0	4.0 - 5.0	5.0 - 6.0	6.1 - 6.6
(NW+SE/NE+SW)							
Ratio ^a	0.209	0.097	0.235	0.135	0.279	0.321	0.170
Error ^b	0.029	0.005	0.028	0.033	0.055	0.126	0.070
Wings Luminosity ^c (10^{39} ergs ⁻¹)				2.41	1.93	1.97	
Error (10^{39} ergs ⁻¹)				0.20	0.21	0.28	
% of Total Wings Luminosity ^d				91.4	79.3	67.2	
Luminosity ^e (10^{39} ergs ⁻¹)				2.59			
Error (10^{39} ergs ⁻¹)				0.20			
% of Total Luminosity ^f				36.8			

Notes.

- ^a Ratio of total counts in both the cross-cone regions with the total counts in both the cone regions.
- ^b Propagated error for the ratio of counts in the cross-cone regions with the counts in the cone regions.
- ^c Luminosity of the extended counts in each of the hard energy bands from the unabsorbed flux in the wings (2"- 15").
- ^d Percentage of the extended hard luminosity compared to the total luminosity, in each energy band in the wings (2"- 15").
- ^e Luminosity of the extended counts in each of the hard energy bands from the unabsorbed flux in the radial range 0"- 15".
- ^f Percentage of the extended hard luminosity compared to the total luminosity, in each energy band in the radial range 0"- 15".

Therefore A is given by the count rate, the effective area of Chandra in the energy band given to PIMMS, and the energy. E is the energy and γ is the photon index, which was set to 2. The count rate was computed as the counts divided by the total cleaned exposure time of the merge. The appropriate energy bins were used each time. All values except for the count rate were assumed to have no errors. The count rate has errors from \sqrt{counts} . The total luminosity in the 2.0 keV - 10.0 keV energy band is 7.5×10^{40} erg s⁻¹ (Levenson et al. 2006). Therefore the percentage of the total luminosity which is extended in the hard band is $\sim 3.5\%$. The percentage of hard band counts which are extended in the wings (2" to 15") relative to the PSF is $\sim 460\%$ which shows that there is ~ 4.6 times the amount of emission from these extended regions as was previously believed. Also in this same wings region, the percentage of extended hard band counts relative to all of the hard band observation counts is $\sim 79\%$ which shows the importance of these discoveries because this was previously thought to be 0%. From Table 3 it can also be seen that when you account for the nuclear source as well as the wings, the counts, and therefore the luminosities, show that only the 3.0 keV - 4.0 keV energy band is extended. This is why there are no values for the 4.0 keV - 5.0 keV and 5.0 keV - 6.0 keV energy bands. This is because, as can be seen in Figures 18a-d, the nuclear source of these energy bands is not extended and the wings are only extended by a small amount.

It can also be seen from Table 3 that the ratio of cross-cone to cone counts in the hard band increases with increasing energy. This is likely due to outlier line emission from the soft band leaking into the hard band. This line emission is from the cone region and therefore as this emission in the cone decreases, the ratio of cross-cone to cone emission will increase.

5.3 Profile Width Trends

In ESO 428-G014 the trend is that the FWHM of the radial profiles decreases as the energy increases (Fabbiano et al. 2018). This is also the case in NGC 3393 at half maximum

and at 3 dex below the maximum. However, the FW3dex gradient is shallower in the cross-cone than in the cone. This could be due to there being different distributions of molecular clouds in the cone directions compared to the cross-cone. Figure 20 suggests that there could be a clump of clouds at a larger distance (e.g. $\sim 30''$ (~ 8.4 kpc)) in the cone, then another clump at a closer distance (e.g. $\sim 13''$ (~ 3.6 kpc)), etc., down to $\sim 5''$ (~ 1.4 kpc). However in the cross-cone, while there is some distribution of clouds, there is much less spread in the distribution, as they all lie between $\sim 5''$ (~ 1.4 kpc) and $\sim 10''$ (~ 2.8 kpc). For the cross-cone emission, if the torus were to have a clumpy structure, with holes in-between the clouds, then I would expect the soft and hard band cross-cone emission to be equal as they would pass through the holes and get scattered in ISM clouds beyond the torus, assuming there was an equal ratio of CT to non-CT clouds. However, this is not observed. Therefore instead of holes, there must be differing optical thicknesses of the clouds within the torus which allow for the hard emission to travel straight through and get Compton scattered towards us and the soft emission to undergo photoelectric absorption.

Similar to ESO 428-G014, this trend suggests that the CT clouds responsible for the hard emission are both more distant and closer to the nuclear source than previously believed. There is soft X-ray extent at larger distances away from the emission source. This means that these dense clouds which are close to the nucleus have a clumpy structure otherwise the soft emission would be absorbed.

In ESO 428-G014 the ratio of FWHM cross-cone to cone values is constant with energy at ~ 1.7 . However in NGC 3393 the FWHM ratio increases from ~ 1.6 to ~ 2.2 , and the FW3dex ratio decreases from ~ 2.8 to ~ 1.0 both with increasing energy. This could mean that the host disk inclination effect, suggested by Fabbiano et al. 2018, is not applicable in the case of NGC 3393.

5.4 Torus Transmission

The volume of the cross-cone regions is ~ 0.7 times that of the cone regions. This is largely due to the generous cone angle used to allow for confident detections in the cross-cone. By using a ratio of 0.235 cross-cone to cone counts (see Table 3), this means that the torus transmits 34% of the amount of emission which the cone regions emit. This is ~ 3 times larger than the transmission of the torus in ESO 428-G014 (Fabbiano et al. 2018) even though their cross-cone volume is ~ 5 times their cone volume. This suggests that there is a range of structures (varying distributions of molecular clouds of varying column densities) which the torus can take.

6 CONCLUSIONS

- (1) In the cone and cross-cone regions of the soft band (0.3 keV - 3.0 keV) of NGC 3393 the X-ray emission is extended, confirming previous results by Levenson et al. (2006). In the bi-cones this is likely due to the narrow line region being photoionised and recombining as a result of the X-rays from the corona. The cross-cone extent suggests a clumpy torus structure. The clouds in this narrow line region and some clouds in the clumpy torus have a column density of $N_H < 1.5 \times 10^{24} \text{ cm}^{-2}$ because the hard (3.0 keV - 6.0 keV) X-ray photons travel through them.
- (2) In the cone and cross-cone regions of the hard band (3.0 keV - 6.0 keV) of NGC 3393 the X-ray emission is extended. This means that there must be clouds of dense material, with a column density $N_H \geq 1.5 \times 10^{24} \text{ cm}^{-2}$ to allow for the hard X-ray photons to be scattered towards our line of sight. Some of these clouds reside close to the nuclear source ($\geq \sim 300 \text{ pc}$) meaning that ESO 428-G014 is not an isolated case (Fabbiano et al. 2018). There is also extent at larger distances, up to $\sim 1.9 \text{ kpc}$, in this cone region meaning that the dense clouds also reside at this distance. The cross-cone regions are also extended although only in select energy bands at select radii. This extent could be a result of a clumpy torus with clouds of low column density allowing the hard X-ray photons to travel through but it could also be due to hot X-ray bubbles which reside in the cross-cone according to simulations of the radio jet interacting with the molecular disk of the galaxy as carried out by Mukherjee et al. (2018).
- (3) The trend of the FWHM of the radial profiles for NGC 3393 is that it decreases as the energy increases. This is also true for the FW3dex. The FW3dex gradient is shallower in the cross-cone than in the cone due to different distributions of clouds. Due to a varying distance of clouds as energy increases, the holes in the torus must not be a vacuum and instead have varying levels of column density. The extended hard emission in the cone direction suggests that there are dense ISM clouds close to the nuclear source.
- (4) The torus in NGC 3393 transmits 34% of the amount of emission which the cone regions emit. Along with ESO 428-G014, we now have a range of transmission values for the torus of an AGN, between $\sim 10\%$ and $\sim 34\%$.

6.1 Future Work

Future work should include increasing the number of AGNs which show potential for having extended emission in the hard continuum. These AGNs should be Seyfert Type IIs and have extended O[III] in the optical because this is a good indicator of extended soft emission in general and therefore hopefully there would also be some extended hard emission. Some example of these candidates are Markarian 3, NGC 1386 and extend the work on Markarian 573 which has been started by (Paggi et al. 2012). Extended hard emission is a relatively new discovery and therefore more galaxies are required to investigate recent discoveries which can help test clumpy torus models.

6.2 Acknowledgements

I thank my supervisor at the Center for Astrophysics | Harvard & Smithsonian, Giuseppina Fabbiano for her support and guidance on this project. I thank Martin Elvis and Peter Maksym for discussion on Compton Thick AGNs and teaching of the CIAO interface. I thank Alessandro Paggi and Mackenzie Jones for discussion on the full width half maximums of the profiles. I also thank Smithsonian Astrophysical Observatory for their funding.

REFERENCES

- Antonucci R., 1993, ARAA, 31, 473
 Arévalo P., Bauer F.E., Puccetti S., et al., 2014, ApJ, 791, 81
 Barvainis R., 1987, ApJ, 320, 537
 Bauer F.E., Arévalo P., Walton D.J., et al., 2015, ApJ, 812, 116
 Carter C., Karovska M., Jerius D., et al., 2003, ASPC..295, 477, ASPC..295
 Comastri A., 2004, ASSL..308, 245, ASSL..308
 David L.P., Jones C., Forman W., et al., 2006, ApJ, 653, 207
 Davis J.E., Bautz M.W., Dewey D., et al., 2012, Space Telescopes and Instrumentation 2012: Ultraviolet to Gamma Ray, 84431A, SPIE.8443
 Fabbiano G., Elvis M., Paggi A., et al., 2017, ApJ, 842, L4
 Fabbiano G., Paggi A., Karovska M., et al., 2018, ApJ, 855, 131
 Fabbiano G., Siemiginowska A., Paggi A., et al., 2019, ApJ, 870, 69
 Fruscione A., McDowell J.C., Allen G.E., et al., 2006, Society of Photo-Optical Instrumentation Engineers (SPIE) Conference Series, 62701V, SPIE.6270
 Koss M.J., Romero-Cañizales C., Baronchelli L., et al., 2015, ApJ, 807, 149
 Kraemer S.B., Crenshaw D.M., Hutchings J.B., et al., 2000, ApJ, 531, 278
 Levenson N.A., Heckman T.M., Krolik J.H., et al., 2006, ApJ, 648, 111
 Li J., Kastner J.H., Prigozhin G.Y., et al., 2004, ApJ, 610, 1204
 Maiolino R., Salvati M., Bassani L., et al., 1998, AA, 338, 781
 Maksym W.P., Fabbiano G., Elvis M., et al., 2016, ApJ, 829, 46
 Maksym W.P., Fabbiano G., Elvis M., et al., 2017, ApJ, 844, 69
 Maksym W.P., Fabbiano G., Elvis M., et al., 2019, ApJ, 872, 94
 Marinucci A., Risaliti G., Wang J., et al., 2012, MNRAS, 423, L6
 Matt G., Brandt W.N., Fabian A.C., 1996, MNRAS, 280, 823
 Mo H., van den Bosch F., White S., 2010, Galaxy Formation and Evolution, 1, 623.
 Mukherjee D., Bicknell G.V., Wagner A.Y., et al., 2018, MNRAS, 479, 5544
 Netzer H., 2015, ARAA, 53, 365
 Paggi A., Wang J., Fabbiano G., et al., 2012, ApJ, 756, 39

- Rees M.J., 1984, ARAA, 22, 471
Theureau G., Bottinelli L., Coudreau-Durand N., et al., 1998,
AAS, 130, 333
Wang J., Fabbiano G., Risaliti G., et al., 2011, ApJ, 729, 75
Zamaninasab M., Clausen-Brown E., Savolainen T., et al., 2014,
Nature, 510, 126